Modeling the Gamma-Ray Spectrum of Cs-137 with NaI (TI) Scintillator

Immanuel Adewumi – 11th Feb 2021

Abstract— **In this study we demonstrated the effects of Compton-scattering both within and outside a common NaI (TI) scintillation detection device. We used the Klein-Nishina formular which relates differential cross-sectional collision angle to determine the probability of photon collisions within the scintillation detector and demonstrated that such a detector can be used to model the real distribution of a radioactive Cs137 gamma-ray source. Using Monte-Carlo numerical Methods for smearing ideal values we were also able to show that the model does produce quite realistic results which look very similar to real NaI (TI) gamma-ray detection data.**

I. Introduction

Gamma-ray spectroscopy is a technique for analysing gamma-ray emission spectra of materials which is heavily employed in fields of nuclear science, medicine, astrophysics, and geochemical research for its usefulness in gamma-ray imaging and determining the nuclear composition of radioactive materials. This report was aimed at modelling the gamma-ray emission spectrum for Cesium-137 using Compton-scattering, Monte-Carlo numerical techniques and the Klein-Nishina formula [1] for calculating the differential cross-section of photons scattered off single free electrons. Within the x-ray and gamma regions the Klein-Nishina formula reduces to Compton-scattering. Since gamma-ray spectroscopy relies heavily on the use of Compton-scattering, and Cs-137 is a gamma source, this was our motivation for its use.

II. Theory

A. Compton Effect

The Compton-Effect **(1923)** discovered through observation by Nobel-laureate Arthur H. Compton is theoretical quantification of the wave-particle duality of matter. By following the laws of energy conservation and using relativistic collision laws for inelastic scattering the equation can be derived. In simplest terms it describes how photons interact with loosely bound electrons of an atom transferring energy which excites them out of their bound states. The collision is inelastic because on interaction photons lose energy. The equation is given by [2]:

$$E_\gamma(\theta) = \frac{E_{\gamma 0}}{1 + \frac{E_{\gamma 0}}{m_e c^2}(1 - \cos(\theta))} \quad (1)$$

where θ is the scattering angle, m_e is the electron rest-mass, c the speed of light in a vacuum and $E_{\gamma 0}$ and $E_\gamma(\theta)$, the photon energies before and after collision.

B. Cesium – 137 gamma-source

Cesium-137 undergoes the radioactive decomposition outlined in Figure 1 [3].
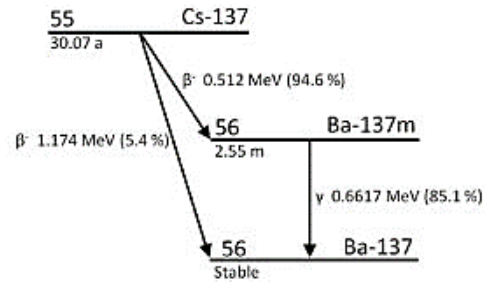
**Fig. 1:** Shows the radioactive decay modes for Cs-137. In public domain.

The unstable $^{55}Cs_{137}$ atom decays by emitting β-particle, with half-life 31.17 years. 94.6% of the time this occurs, the β-particle carries away an energy 512 keV, and the $^{55}Cs_{137}$ in turn transmutes to become an unstable (or meta stable) state of $^{56}Ba_{137}$ (Barium137) with weight 137 atomic mass units. The unstable state of barium is denoted in the diagram with the letter m which stands for meta-stable. It decays with a half-life of 2.55 minutes to Ba-137 stable ground-state, by emitting a gamma ray with characteristic energy 661.7 keV [4].

C. NaI (TI) – Scintillation Detector

There are 2 major detectors tyoes: scintillation and semi-conductor-based detectors. Though the latter yield much higher resolution, the accessibility of scintillators means they are more widely used. The NaI (TI) thallium-doped sodium-iodide scintillator was used in this study to measure the gamma emission of $^{55}Cs_{137}$.

1) Detector Composition

These detectors are composed of 2 major compartments. The scintillator and the photomultiplier-tube shown in Figure 2 [5] below.
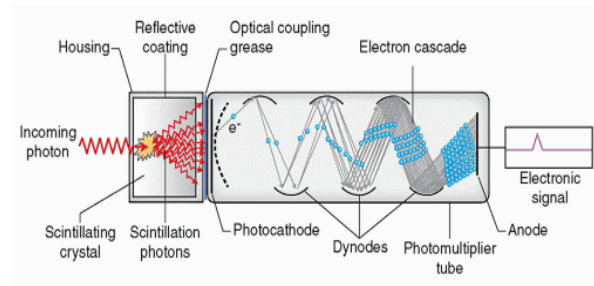
Fig. 2: An NaI (TI) scintillation detector with all its parts labelled.

2) Scintillator

It functions as follows, within the scintillator incident gamma-ray photons interact with the thallium-doped sodium-iodide (NaI (TI)) crystals, and these consequently cause the crystal to fluoresce (emit visible-light). The lower energy photons with frequencies within the visible region are created due to the thallium and iodine doping within the sodium-iodide crystals. This creates valence bands within what would otherwise be known as the "forbidden" region for pure Na metal (in which electrons previously could not inhabit). Shown in Figure 3 [6] below.
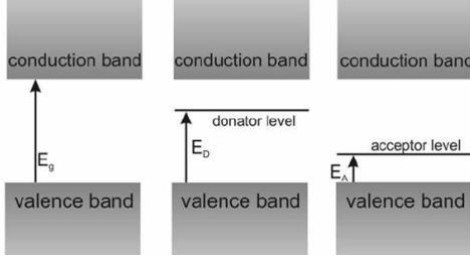
Fig. 3: Shows a model of the effect which doping has on the metals used in scintillator crystals. What is called a donator band is created within the "forbidden-region" E_g between the valence and conduction band

For a pure metal, the "forbidden-region" or gap E_g between the valance and conduction bands is larger, but the probability of de-excitation of electrons after excitation by incident gamma-photons is much lower. Thus, it is a much less efficient process than that of doped NaI. Iodine doping creates a higher number of bands for each excited electron to fall back to; thus, increasing the probability of photon emission due to de-excitation. The number of visible-light photons emitted from the NaI (TI) is proportional to the amount of gamma photons incident on it.

3) Photomultiplier-tube

The generated visible-light photons then strike the photoelectric cathode within the photomultiplier-tube, emitting electrons which are accelerated towards the dynodes. They strike these repeatedly, as shown in Figure 3 displacing an increasing number of electrons, to amplify the electric signal. At the end of the tube, they are collected by the anode, which measures an electric pulse signal and displays it on an MCA (multichannel analyser).

4) Detector Signal

In the ideal world, a mono-energetic gamma signal would be detected as a a single (Dirac-delta) frequency function (of infinitesimal width) on the scintillation device. In, practice however, the fluctuations in light output from the photoelectric phosphor and the statistical nature of the events occurring in the photo-multiplier tube, detector-measured monoenergetic signals are smeared out statistically by a gaussian function distribution is what is seen on the analyser, and the detector resolution is defined as the FWHM – full-width at half-maximum of the Gaussian distribution. Figure 4 [7] shows a sketch of this.

The justification for a Gaussian smearing is as follows; if monoenergetic photons were incident on the photocathode and it emitted an electron for every photon, though these electrons are accelerated towards the dynodes and ultimately the anode, statistically not all electrons would reach it. Thus, this poses a problem for statistical handling.

There are 2 probabilities, p is the probability that an electron generated at the photocathode reaches the anode, strikes it and is detected, $1-p$ represents the probability that it does not but gets lost in random scattering within the tube. With 2 possible outcomes this can be described as a binomial process, with mean np and variance $np(1-p)$. If the anode has a small collision cross-section and p is very small, its variance is approximately equal to its mean, $np \approx np(1-p)$ which is the condition for a Poisson distribution. Finally, Central-Limit-Theorem [9] shows that for a large number of sample-measurements, the distribution of the mean of these samples tends to a Gaussian-curve.
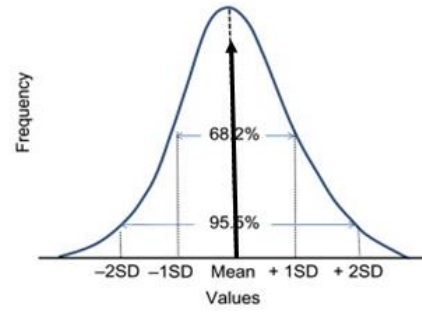
Fig. 4: A diagram of a Gaussian-smeared Dirac-delta function.

D. Klein-Nishina Equation

Within gamma-ray scintillation-detectors not all photons incident on the crystal-lattice are absorbed by it, some are themselves Compton-scattered within the detector, striking it at a non-zero angle and depositing only a fraction of their energy to the electrons within the NaI (TI) crystal. This results in additional signal distributions other than the monoenergetic photopeak being measured.

The Klein-Nishina formula (2) [10] developed by Yoshio Nishina and Oskar Klein **(1929)** gives the differential cross-section of photons which have been scattered by single free-electrons. This formula was useful for modeling and estimating the results of the Compton-scattering which occurred within the detector itself. It is shown below.

$$\frac{d\sigma}{d\Omega} = \frac{1}{2}\alpha^2 r_c^2 P(E_\gamma,\theta)^2 \left[P(E_\gamma,\theta) + P(E_\gamma,\theta)^{-1} - sin^2(\theta)\right] \quad (2)$$

Above, in equation (2). $d\sigma/d\Omega$ is the differential cross-section, with $d\Omega$ being the infinitesimal solid-angle in steradians subtended by the line-of-sight of the scattering centre point (shown in Figure 5 [11]), $P(E_\gamma, \theta) = E_\gamma(\theta) / E_{\gamma 0}$; is the ratio of energy of the scattered photon to the incident photon and can be gotten by dividing through the equation (1) for Compton-scattering by $E_{\gamma 0}$, α is the fine-structure constant (~1/137.04) and $r_c = \hbar/m_e c$ is the reduced Compton wavelength of an electron. With m_e being the rest electron mass of (~511 keV/c^2), and θ being the scattering angle.
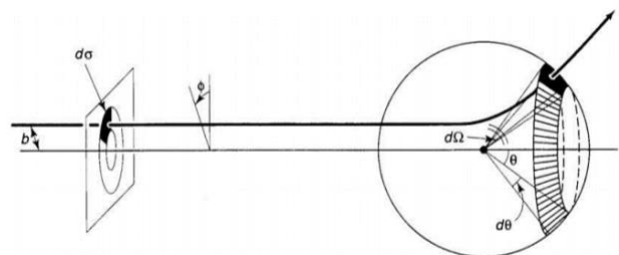

Fig. 5: A diagram showing the concept of the differential cross section for a particle on a collision course, $d\sigma$ is the cross section $d\Omega$. The infinitesimal solid-angle and b the impact parameter.

III. EXPERIMENTAL METHOD

Compton-scattering experiments require a radioactive gamma source, a reflector, and a detector. As stated in previous sections the NaI (TI) scintillation-detector was used. An aluminium block was used for the reflector. The study focused on the numerical aspects as prerecorded data was provided. The experimental set-up is shown (both schematic and real) in section *A* to give deeper insight into the mechanisms of the Compton-scattering within the measuring apparatus.

A. Set-up

The configuration for the set-up can be seen in the schematic diagram Figure 6 [12].
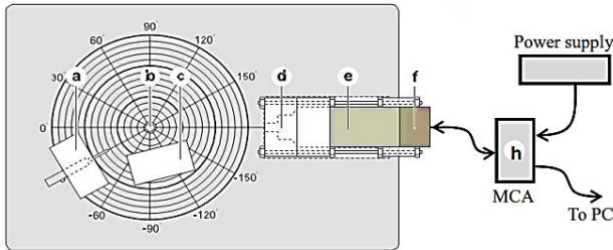
Fig. 6: Shows a schematic of the set-up gotten from the 3rd year labs E3 Imperial College Physics lab manual. The radioactive sample-holder represented by (a), (b) the aluminium scaterrer, (c) protective lead-block, (d), lead-shielding for the scintillator aperture, (e) scintillator and photomultiplier, (f)anode, and (h) MCA-multichannel analyser.

The source is a radioactive sample positioned within a sample-holder (a), which is in-turn placed on a rotatory platform with angles marked in degrees. At the centre of the platform is a cylindrical aluminium rod (b) reflector (scattering target). In front of it, (at the face of scattering) there is a thick block of lead Pb (c) placed for shielding (absorbing excess gamma-rays) and thus protecting the experimenter from unsafe levels of exposure.

The degree markings on the platform, through which the source sample-holder can be rotated, measure the scattering angle θ. At the other end of the rotatory platform the entrance aperture of the detector (d) is positioned at a fixed point close to the edge of the platform circumference. This entrance aperture is encased in a lead box to keep out external background radiation. Part (e) houses the scintillator and photomultiplier tube whose functions have been detailed in earlier sections, and electric signals generated at the detector anode are measured at the MCA (h) Multichannel analyser device which is connected to a PC monitor or display screen.

Below in Figure 7 [13] is an image taken of the real experimental set-up.

Fig. 7: Snapshot of the NaI (TI) Scintillar set-up taken by Steve Kolthammer at Imperial College London department of Physics.

B. Calibration

The scintillation-detector does not measure the exact energy-amplitude of the source but gives a reading proportional to it. Thus, equipment calibration was done using 4 elements of known characteristic gamma energies, Na^{22} - 511.0034 keV, Mn^{54} – 834.827 keV, Cs^{137} – 662 keV, Am^{241} – 59.6 keV.

1) Removing background radiation

First the equipment was set-up (at the 0-degree angle) without a radioactive source and no aluminium scattering rod in place. In this configuration the detector was allowed to run for 100 s to take measurements of the background radiation. The equipment was then kept at 0 degrees (direct line of sight) between source and detector, with no aluminium scatterer, and each of the 4 radioactive gamma sources were positioned in the sample-holder with detector-readings taken for 100 s each. The measured background-radiation was deducted from each of the 4 gamma measurements for more reliable readings of the true gamma-emission spectra for the sources.

2) Curve-fitting and Uncertainties

Since the measured amplitude of each photon is a proxy for its energy (with an expected proportionality relation), plotting the amplitudes against frequency (photon-count) for each element gives the amplitude-locations for their gamma photopeaks. As explained in the theory section the measured photopeak signals observed were indeed gaussian-shaped, with the mean (gaussian-centre) indicating the amplitude-value for the characteristic gamma photopeak.

The uncertainty for each data-point was estimated as the square-root of the frequency value (photon-count) since each measurement was an independent event and assumed to be fundamentally Poisson distributed, as explained in the theory section. The measured photo-peak was fit using a non-linear regression fitting algorithm and its parameters (mean and Full-width-at-half-maximum FWHM) were determined. The Poisson-based uncertainties were used to weight each data-point during the fitting process, for more accurate results. Thermal-Doppler peak-broadening was discarded as a possible source of uncertainty due to the much greater order of magnitude for the energy values of Gamma-rays.

3) Graphing

Below in Figure 8 is the curve-fitted graph, using Python programming language for Americium241 the lowest energy element. The left side of the data-point distribution seemed to be higher than the right, and so a function defined by a Gaussian added to a straight-line with negative slope gradient was used for the curve-fitting algorithm, to produce more reliable results for the peak-mean (amplitude) value. The Voigt-profile (a convolution of Gaussian and Lorentzian fit) which accounts for thermal broadening was fit (purple-line) alongside a Gaussian fit (blue line). The results show that within estimated errors there is negligible difference between

the values gotten for the Voigt and Gaussian fit, further denoting an insignificant effect of thermal on the estimated results.
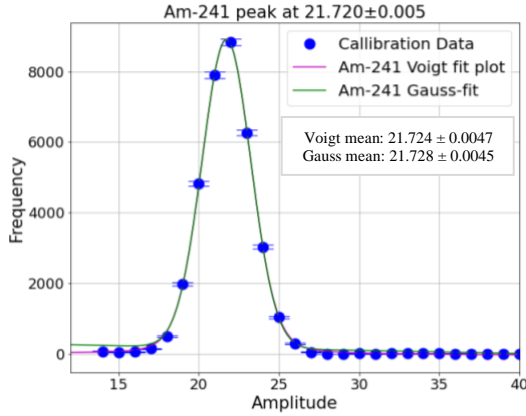
Fig. 8: Shows Am²⁴¹ Peak-position for the Voigt (purple) and Gauss (green) fits. The Poisson-estimated errors for some of the data-points can also be seen. The Voigt and Gauss means 21.724 ± 0.0047 and 21.728 ± 0.0045 respectively, lie within 1-standard deviation of each other, thus are in agreement.

4) Determining Amplitude-Energy Conversion

The processes in the previous steps *(2)* and *(3)* were repeated for all other radiation sources. The errors of each element's peak-positions were gotten from the covariance matrix given by the curve-fitting algorithm. By plotting the measured amplitude peak position for each element against their known emission energies we expected to find a linear fit whose equation would be the amplitude-energy conversion equation for our given set-up. This is indeed what was observed. Table I shows the measured amplitudes against the known gamma energies of each element. Using the peak-position errors estimated above the points were weighted, and the best-fit was determined using a 1-dimensional least-squares linear-regression fit. The resulting Amplitude-Energy conversion equation (3) is shown below and had a percentage uncertainty of 0.8%

$$E = 3.53 \times A - 17 \qquad (3)$$

Here, E stands for true energy and A is the measured amplitude.

C. Compton Scattering - Verification

For Cs¹³⁷ the experiment was repeated at angles 0°, 20°, 30° and 45°. For the zero-degree angle the original data and background radiation was deducted. At higher angles, background radiation readings were taken. Each measurement was run for a duration of 100 s each, except the 45° angle, which was run for 300 s. As, in the previous

section the background radiation data was deducted from the Compton-scattering measurements and plots were gaussian-fitted to determine peak-position using Python. The code was updated to include the Amplitude-Energy conversion within the curve-fit process.

To verify the existence of Compton-scattering, we plotted the inverse energies for scattered photons $1/E_\gamma$ at each angle against the cosine of their angles. The Compton-scattering equation (1) predicts a linear relationship between these two variables with a negative gradient of $-1/m_e c^2 = -1.23 \times 10^{13}$ J. Indeed, this is what was observed, a straight-line with a gradient of $(-1.25 \pm 0.03) \times 10^{-13}$ J, in agreement with literature values.

IV. RESULTS AND ERRORS

A. Monte-Carlo Preliminary Results

As a preliminary experiment we tested the use of Monte-Carlo numerical methods in simulating the peaks with known Gaussian distribution. By taking random seeds chosen between probability 0 and 1 and using the Inverse error function to smear out a Dirac-delta (single-valued point) of known gamma-energy 662 keV, we were able to simulate the Gamma photopeak very closely for Cs-137. The number of simulation points determined the Gaussian height and so a proper scaling factor which minimized this distance was chosen numerically.

For the peaks at other angles 20°, 30° and 45° respectively an appropriate scaling factor was chosen, using the relative-height scales of the various peaks within real experimental data. The graphs for each angle can be seen below in Figures 9, 10, 11 and 12. We also noted that the true FWHM (peak resolutions varied as the root of the mean(peak-position) this was used in all further simulations.
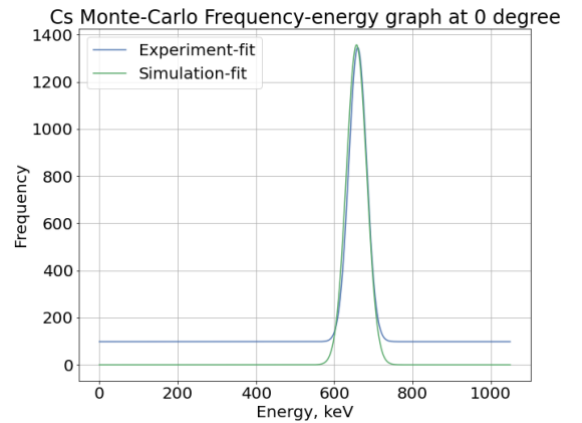
Fig. 9: Shows the Gaussian-fit data plotted alongside the Monte-Carlo simulation for Cs-137 at 0°.
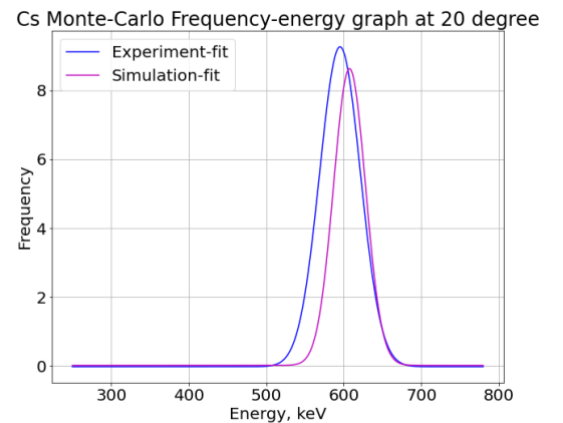
Fig. 10: Shows the Gaussian-fit data plotted alongside the Monte-Carlo simulation for Cs-137 at 20°.

TABLE I
ENERGY-AMPLITUDE CONVERSION

Element	Literature Energy (keV)	Amplitude Measurement	Uncertainty
Na-22	511.0	150.0	0.11
Mn-54	834.8	238.8	0.29
Cs-137	662.0	192.08	0.04
Am-241	59.6	21.74	0.01

TABLE I: Shows literature Energies against the measured amplitudes of radioactive elements Na²²- 511.0034 keV, Mn⁵⁴ – 834.827 keV, Cs¹³⁷ – 662 keV. Am²⁴¹ – 59.6 keV. and the measurement uncertainties.
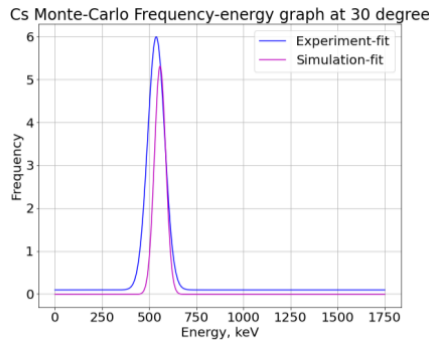
Fig. 11: Shows the Gaussian-fit data plotted alongside the Monte-Carlo simulation for Cs-137 at 30°.

B.   Monte-Carlo Simulation of Cs-137 Spectra

For the full spectrum of Cs-137 the distribution was carefully analysed and modeled based on known features of Cs-137 itself and its interaction with NaI (TI) scintillator.

1)   Gamma and X-ray Photopeaks

The main characteristic gamma peak of Cs^{137} was the 662 keV peak however there was another quite dominant peak at around **23 keV []**. This peak is due to X-ray fluorescence, which is a phenomenon that occurs within the decay process of Cs-137 when its daughter nucleus Ba-137 loses an atomic electron.

2)   Lead Peaks

Some of the high-energy photons are known to strike the lead-shielding of the scintillator, exiting k-orbital electrons and, which in-turn cause x-ray emissions at their de-excitation. There are 3 characteristic lead x-rays of 73, 75 and 85 keV, respectively. Though they are not resolvable by NaI (TI) equipment a significant a peak around the 72 keV Pb x-ray region was observed. It was modelled as 2 Dirac-deltas, one at 74 keV (average of the 73 and 75 keVs) with a detector resolution (FWHM) of 2 times the square-root of the mean 74 keV, whilst the other at 85 keV was modelled with the regular root of the mean.

3)   Compton-Shelf & Peak

Shortly to the left of the gamma photopeak there is a shallower peak which is followed by a convex shape shown in the real data. This is the region of Compton-scattering within the detector itself and is well modelled using the Klein-Nishina model for estimating electron and photon cross sections.

The right-most peak with the highest energy corresponds to the single-scattered electrons which collide with the scintillator and are scattered backwards at an angle of 180 degrees. This point is known as the Compton-Edge or Compton-shelf and has a sharp cut-off. The peak closer to the left is known as the Compton-Peak (or backscatter Peak) and corresponds to the photons which are Compton-scattered in 2 or more scattering events before absorption within the scintillator. Below in Figure 13 **[ ]** shows the typical shape of an NaI (TI) recording of Cs^{137} gamma emission spectrum.

4)   Monte-Carlo Modelling

Within the model, as was done in the earlier parts of the simulation, the known gaussian-distributed gamma and x-ray peaks were modeled within the Monte-Carle simulation, using discrete Dirac-deltas positioned at each characteristic
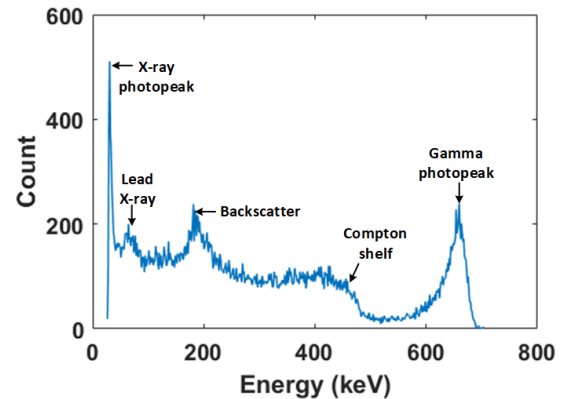

Fig. 13: Shows the typical gamma emission spectrum for Cs^{137}.

energy and smeared with a probabilistic gaussian function. The Compton shelf-to-peak region was modelled using the Klein-Nishina function mentioned earlier.

The Compton-scattering events which occur within the scintillator crystal could be viewed as a cloud of photons and electrons with different probabilities of collision, dependent on impact energies and collision angles. Since the Klein-Nishina function is a measure of differential cross-section available to photons incident on electrons at various angles it serves also as a measure of the probability distribution for the photons colliding with electrons at these angles. To permit its use in modelling the Compton-shelf of our Energy by Photon-count frequency graph, the Klein-Nishina equation (2) for impact photons was rearranged using Compton-scattering equation (1) and it was rewritten in-terms of impact energies.

It was normalized and its complement, cross-sectional area for electrons colliding was gotten using 662-E_p keV as the energy argument within the same Klein-Nishina equation (2). Here, E_p represents the photon energy within the scintillator before Compton-scatter. 662 keV is used because that is the maximum energy for displacements and collisions introduced by the monoenergetic gamma photons.

The Figure 14 shows the Klein-Nishina distributions for photons and electrons as well as their sum (which are the true values which model the Compton-region). For illustrative purposes they have been plotted on the same graph, with the x-axis showing the true energy of incident photons, but the energy of the electrons (green-line) is 662-E_p, 662 minus the corresponding Energy on the graph.
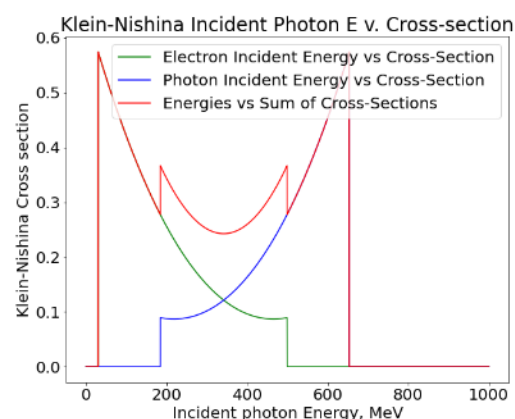

Fig. 14: Shows the Klein-Nishina cross-sections of the electrons(green) and photons(blue) and their sum(red).

Unlike the graph, above the Compton-shelf is only defined within the regions where the two electron and photon cross-section graphs overlap. The parts overshooting these regions are not as significant because on the left of the overlap, for electrons, though there is larger collision-cross-section for energies close to zero, the energies are so low that their likelihood of being detected falls to zero. The right diminishes for similar reasons, photons of near-zero energy have very low likelihood of exciting electrons out of even weakly bound states within the scintillator crystal.

The photon counts recorded in these regions were, however, still significantly above the background level and where relatively flat. For this reason, both regions were modelled with Heaviside-step functions added to slowly varying quadratics. After appropriate scaling, each data-point within these regions and the Compton-region were treated as Dirac-delta functions (discrete values) and individually smeared with Gaussian probability function.
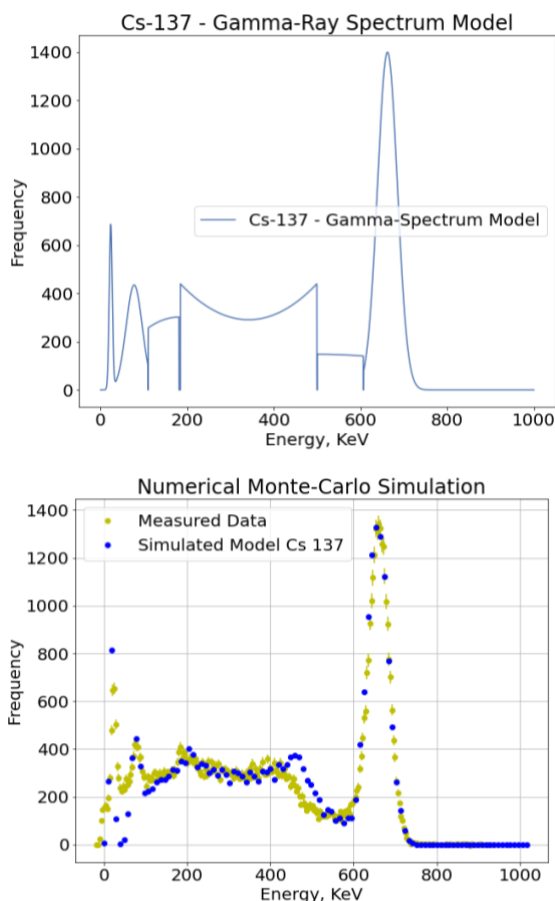
Fig. 16: Shows the Monte-Carlo simulated points (blue) plotted against the real measured data (yellow) for the Cs^{137} NaI (TI) gamma-spectrum.

Results of the theoretical modelling, and Monte-Carlo simulation are shown above in Figures 15 and 16, respectively. For aided graphical representation, the photopeaks have been plotted as their full Gauss-shaped

functions (though Dirac deltas were used in the actual simulation.

The results showed that all peaks, identified within the gamma spectrum for Cs^{137} could be well, modelled using Dirac-deltas smeared with Gaussian-probability curves, and that the Compton-region of internal Compton-scattering within the scintillator-crystal could be well modelled using the Klein-Nishina cross-sectional equation for photons incident on free-electrons. There was only a significant deviation of the simulation points (seen in Figure 16) from the true data around the sharp cut-off described as the Compton-Edge. A possible reason might be due to the electrons within the crystal not being completely free.

V. CONCLUSION & DISCUSSION

In this study we demonstrated the effects of Compton-scattering both within and outside a common NaI (TI) scintillation detection device. We used the Klein-Nishina formular which relates differential cross-sectional collision angle to determine the probability of photon collisions within the scintillation detector and demonstrated that such a detector can be used to model the real distribution of a radioactive Cs^{137} gamma-ray source. Using Monte-Carlo numerical methods for smearing ideal values we were also able to show that the model does produce quite realistic results which look very similar to real NaI (TI) gamma-ray detection data.

An improvement on this experiment could involve the use of higher resolution Germanium (semiconductor) detectors.

REFERENCES

[1] J. S. Turner, "New directions in communications," *IEEE J. Sel. Areas Commun.*, vol. 13, no. 1, pp. 11-23, Jan. 1995.

[2] W. P. Risk, G. S. Kino, and H. J. Shaw, "Fiber-optic frequency shifter using a surface acoustic wave incident at an oblique angle," *Opt. Lett.*, vol. 11, no. 2, pp. 115–117, Feb. 1986.

[3] P. Kopyt *et al.,* "Electric properties of graphene-based conductive layers from DC up to terahertz range," *IEEE THz Sci. Technol.,* to be published. DOI: 10.1109/TTHZ.2016.2544142.

[4] R. J. Hijmans and J. van Etten, "Raster: Geographic analysis and modeling with raster data," R Package Version 2.0-12, Jan. 12, 2012. [Online]. Available: http://CRAN.R-project.org/package=raster

[5] Teralyzer. Lytera UG, Kirchhain, Germany [Online]. Available: http://www.lytera.de/Terahertz_THz_Spectroscopy.php?id=home, Accessed on: Jun. 5, 2014

[6] J. O. Williams, "Narrow-band analyzer," Ph.D. dissertation, Dept. Elect. Eng., Harvard Univ., Cambridge, MA, USA, 1993.

[7] N. Kawasaki, "Parametric sastudy of thermal and chemical nonequilibrium nozzle flow," M.S. thesis, Dept. Electron. Eng., Osaka Univ., Osaka, Japan, 1993.

[8] A. Harrison, private communication, May 1995.

[9] B. Smith, "An approach to graphs of linear forms," unpublished.

[10] A. Brahms, "Representation error for real numbers in binary computer arithmetic," IEEE Computer Group Repository, Paper R-67-85

[11] R. Fardel, M. Nagel, F. Nuesch, T. Lippert, and A. Wokaun, "Fabrication of organic light emitting diode pixels by laser-assisted forward transfer," *Appl. Phys. Lett.*, vol. 91, no. 6, Aug. 2007, Art. no. 061103.

[12] J. Zhang and N. Tansu, "Optical gain and laser characteristics of InGaN quantum wells on ternary InGaN substrates," *IEEE Photon. J.*, vol. 5, no. 2, Apr. 2013, Art. no. 2600111